
Optimal Transport on the Manifold of SPD Matrices for Domain Adaptation

Or Yair

Viterbi Faculty of Electrical Engineering
 Technion, Israel Institute of Technology
 Haifa, 3200003, Israel
 oryair@campus.technion.ac.il

Felix Dietrich

Department of Chemical and Biomolecular Engineering
 Johns Hopkins University
 Baltimore, MD 21218-2608, USA
 felix.dietrich@jhu.edu

Ronen Talmon

Viterbi Faculty of Electrical Engineering
 Technion, Israel Institute of Technology
 Haifa, 3200003, Israel
 ronen@ee.technion.ac.il

Ioannis G. Kevrekidis

Department of Chemical and Biomolecular Engineering
 Johns Hopkins University
 Baltimore, MD 21218-2608, USA
 yannis@princeton.edu

Abstract

The problem of domain adaptation has become central in many applications from a broad range of fields. Recently, it was proposed to use Optimal Transport (OT) to solve it. In this paper, we model the difference between the two domains by a diffeomorphism and use the polar factorization theorem to claim that OT is indeed optimal for domain adaptation in a well-defined sense, up to a volume preserving map. We then focus on the manifold of Symmetric and Positive-Definite (SPD) matrices, whose structure provided a useful context in recent applications. We demonstrate the polar factorization theorem on this manifold. Due to the uniqueness of the weighted Riemannian mean, and by exploiting existing regularized OT algorithms, we formulate a simple algorithm that maps the source domain to the target domain. We test our algorithm on two Brain-Computer Interface (BCI) data sets and observe state of the art performance.

1 Introduction

In many applications, the acquired data sets do not reside in the same domain; this gives rise to the need for domain adaptation methods. Here, we focus on the problem of domain adaptation on the cone manifold of SPD matrices. This particular interest arises because SPD matrices have proven to be useful features in many machine learning tasks; see for example works by Pennec et al. [2006], Barachant et al. [2013], Freifeld et al. [2014] and references therein. In addition, SPD matrices represent a broad family; while the use of SPD *covariance* matrices is perhaps the most prominent and widely-spread, there exist other important types of SPD matrices for data analysis, such as kernel matrices, diffusion tensor images, graph-related operators, and many more.

Classical domain adaptation problems arise when data collection or acquisition is performed at multiple sites, with different equipment, under various settings and configurations, etc. As a result, the collected data sets suffer from substantial batch effects, which often lead to poor generalization between the sets despite the informative (common) internal structure of each set individually. Naturally, such batch effects carry over from the data to their (SPD) features.

Following a recent line of work, we use OT for domain adaptation; see for example the paper by Courty et al. [2017] and references therein. While the vast majority of methods implement the OT in

the Euclidean space, in this paper, we carry out OT on the cone manifold of SPD matrices. Note that the Grassmannian manifold could be considered as well in a similar fashion. Our main contributions are as follows.

- Based on the polar factorization theorem of diffeomorphisms on Riemannian manifolds, we present a new analysis, highlighting the advantages and limitations of OT for domain adaptation. Our analysis includes both the general Riemannian setting as well as the particular SPD manifold.
- We propose a well-defined and easy to implement algorithm for domain adaptation with OT on the manifold of SPD matrices.
- We show that the application of the proposed algorithm to two BCI data sets achieves state of the art results.

2 Preliminaries

2.1 Preliminaries on the cone manifold of SPD matrices

We give a brief overview of the Riemannian geometry of the cone manifold of SPD matrices. For more details, we refer the reader to Bhatia [2009]. A real symmetric matrix $\mathbf{P} \in \mathbb{R}^{d \times d}$ is positive-definite if and only if it has only strictly positive eigenvalues. The collection of all SPD matrices constitutes a convex half-cone in the vector space of real $d \times d$ symmetric matrices. This cone forms a differentiable Riemannian manifold \mathcal{P}_d equipped with the following inner product at the tangent space $\mathcal{T}_{\mathbf{P}}\mathcal{P}_d$ (the space of symmetric matrices) at the point $\mathbf{P} \in \mathcal{P}_d$

$$\langle \mathbf{A}, \mathbf{B} \rangle_{\mathcal{T}_{\mathbf{P}}\mathcal{P}_d} = \langle \mathbf{P}^{-\frac{1}{2}} \mathbf{A} \mathbf{P}^{-\frac{1}{2}}, \mathbf{P}^{-\frac{1}{2}} \mathbf{B} \mathbf{P}^{-\frac{1}{2}} \rangle, \quad (1)$$

where $\mathbf{A}, \mathbf{B} \in \mathcal{T}_{\mathbf{P}}\mathcal{P}_d$ are symmetric matrices, and $\langle \cdot, \cdot \rangle$ is the Euclidean inner product operation.

\mathcal{P}_d is a Hadamard manifold, namely, it is simply connected and it is a complete Riemannian manifold of non-positive sectional curvature. Manifolds with non-positive curvature have a unique geodesic between any two points. Specifically, the geodesic between $\mathbf{P} \in \mathcal{P}_d$, and $\mathbf{Q} \in \mathcal{P}_d$ is given by

$$\varphi(t) = \mathbf{P}^{\frac{1}{2}} (\mathbf{P}^{-\frac{1}{2}} \mathbf{Q} \mathbf{P}^{-\frac{1}{2}})^t \mathbf{P}^{\frac{1}{2}}, \quad 0 \leq t \leq 1, \quad (2)$$

see Bhatia [2009]. The arc-length of the geodesic curve defines the following Riemannian distance

$$d_R^2(\mathbf{P}, \mathbf{Q}) = \left\| \log \left(\mathbf{Q}^{-\frac{1}{2}} \mathbf{P} \mathbf{Q}^{-\frac{1}{2}} \right) \right\|_F^2 = \sum_{i=1}^d \log^2 \left(\lambda_i(\mathbf{P} \mathbf{Q}^{-1}) \right), \quad (3)$$

where $\mathbf{P}, \mathbf{Q} \in \mathcal{P}_d$, $\|\cdot\|_F$ is the Frobenius norm, $\log(\mathbf{P})$ is the matrix logarithm, and $\lambda_i(\mathbf{P})$ is the i -th eigenvalue of \mathbf{P} . The Logarithm map from \mathcal{P}_d to $\mathcal{T}_{\mathbf{P}}\mathcal{P}_d$ is given by

$$\mathbf{A}_i = \text{Log}_{\mathbf{P}}(\mathbf{P}_i) = \mathbf{P}^{\frac{1}{2}} \log \left(\mathbf{P}^{-\frac{1}{2}} \mathbf{P}_i \mathbf{P}^{-\frac{1}{2}} \right) \mathbf{P}^{\frac{1}{2}} \in \mathcal{T}_{\mathbf{P}}\mathcal{P}_d. \quad (4)$$

The Exponential map from $\mathcal{T}_{\mathbf{P}}\mathcal{P}_d$ to \mathcal{P}_d is given by

$$\mathbf{P}_i = \text{Exp}_{\mathbf{P}}(\mathbf{A}_i) = \mathbf{P}^{\frac{1}{2}} \exp \left(\mathbf{P}^{-\frac{1}{2}} \mathbf{S}_i \mathbf{P}^{-\frac{1}{2}} \right) \mathbf{P}^{\frac{1}{2}} \in \mathcal{P}_d. \quad (5)$$

The Riemannian mean $\overline{\mathbf{P}}$ of a set $\{\mathbf{P}_i | \mathbf{P}_i \in \mathcal{P}_d\}$ is defined using the Fréchet mean:

$$\overline{\mathbf{P}} = \arg \min_{\mathbf{P} \in \mathcal{P}_d} \sum_i d_R^2(\mathbf{P}, \mathbf{P}_i). \quad (6)$$

This optimization problem (6) is strictly convex and can be solved by an iterative procedure. In Section 3.4, we extend the algorithm presented in Fletcher and Joshi [2004] to compute a *weighted* Riemannian mean. Given a set $\{\mathbf{P}_i | \mathbf{P}_i \in \mathcal{P}_d\}$ and its Riemannian mean $\overline{\mathbf{P}}$, a commonly used Euclidean approximation of the Riemannian distances on \mathcal{P}_d in the neighborhood of $\overline{\mathbf{P}}$ is given by

$$d_R^2(\mathbf{P}_i, \mathbf{P}_j) \approx \|\tilde{\mathbf{A}}_i - \tilde{\mathbf{A}}_j\|_F^2, \quad (7)$$

where $\tilde{\mathbf{A}}_i = \overline{\mathbf{P}}^{-\frac{1}{2}} \text{Log}_{\overline{\mathbf{P}}}(\mathbf{P}_i) \overline{\mathbf{P}}^{-\frac{1}{2}}$.

2.2 Preliminaries on optimal transport on Riemannian manifolds

Let (\mathcal{M}, g) be a smooth, connected, oriented, d -dimensional Riemannian manifold with metric g . Let $c(p, q)$ be the “cost of moving a unit of mass” from point p to point q on \mathcal{M} , and define two finite Borel measures μ_1, μ_2 that are absolutely continuous with respect to the volume form of \mathcal{M} so that they have densities f_1, f_2 . Then, the Kantorovich OT problem consists of finding a transport plan $\gamma^* : \mathcal{M} \times \mathcal{M} \rightarrow \mathbb{R}$ that solves

$$\inf_{\gamma} \int_{\mathcal{M} \times \mathcal{M}} c(p, q) d\gamma(p, q). \quad (8)$$

The infimum ranges over all plans γ with $f_2(p) = \int_{\mathcal{M}} \gamma(p, \cdot) d\text{vol}$ and $f_1(q) = \int_{\mathcal{M}} \gamma(\cdot, q) d\text{vol}$. In our case, we choose the cost function $c(p, q) = d_R^2(p, q)$, where $d_R(p, q)$ is the Riemannian distance between two points $p, q \in \mathcal{M}$ induced by g . This cost function is well-studied in the theory of OT, see Villani [2009], Fathi and Figalli [2010]. In particular, the given assumptions on the measures μ_1, μ_2 result in a unique solution γ^* to (8) that is concentrated on the graph of an invertible function $t : \mathcal{M} \rightarrow \mathcal{M}$ such that $\mu_2(V) = \mu_1(t^{-1}(V))$ for all measurable sets $V \subset \mathcal{M}$.

If the densities of the two measures are sampled at N_1 and N_2 discrete points respectively, they can be represented by vectors $\hat{\mathbf{f}}_1 \in \mathbb{R}^{N_1}$, $\hat{\mathbf{f}}_2 \in \mathbb{R}^{N_2}$. This leads to the discrete version of (8):

$$\min_{\Gamma} \langle \Gamma, \mathbf{C} \rangle, \quad (9)$$

where $\Gamma \in \mathbb{R}^{N_1 \times N_2}$ satisfying $\Gamma \mathbf{1}_1 = \hat{\mathbf{f}}_1$ and $\Gamma^T \mathbf{1}_2 = \hat{\mathbf{f}}_2$. $\mathbf{C} \in \mathbb{R}^{N_1 \times N_2}$ represents the transport cost between the N_1 points in the source set and the N_2 points in the target set.

3 Domain adaptation with optimal transport

3.1 The polar factorization theorem

Instead of starting with two arbitrary measures, assume the measure μ_2 is related to μ_1 through a diffeomorphism $s : \mathcal{M} \rightarrow \mathcal{M}$ such that for all measurable subsets $V \subset \mathcal{M}$,

$$\mu_2(V) = \mu_1(s^{-1}(V)). \quad (10)$$

In the context of domain adaptation that we consider here, the map s represents the change from the source to the target domains. With these prerequisites, we ask: *given only f_1 and f_2 (or, respectively, μ_1 and μ_2), how much of the information in s can be recovered?*

McCann [2001] proved that diffeomorphisms s on Riemannian manifolds have a polar factorization

$$s = t \circ u, \quad (11)$$

where t is the solution to an OT problem between the two measures μ_1 and μ_2 that are related by (10), and $u : \mathcal{M} \rightarrow \mathcal{M}$ is a volume-preserving map such that $\mu_1 = \mu_1 \circ u^{-1}$. The decomposition (11) is unique, because the OT problem has a unique solution t , and thus $u = t^{-1} \circ s$ is also unique (uniqueness is defined up to sets of measure zero, see McCann [2001] for compact manifolds and Fathi and Figalli [2010] for noncompact manifolds). It can further be shown that t is the solution to OT if and only if it can be expressed as the gradient of a function ψ that is c -convex with respect to the cost function c (see Brenier [1991], McCann [2001]).

The polar factorization (11) enables us to present a new insight on domain adaptation. If for a given map s , the map u in (11) is the identity, solving the OT problem recovers the map s . However, if u is not the identity map, solving the OT problem will only recover the function t . This means that the correct target density will be recovered, but the approach will still fail to provide the correct point-wise mapping s between the source and the target domains. The further u is away from the identity map, the more distortion is introduced into the adaptation. Such a “distance” from the identity map can be measured, for example, in the L^2 -norm on the space of smooth functions $C^\infty(\mathcal{M})$ on the manifold. For more details, see Modin [2017].

3.2 Domain adaptation in a Euclidean space

When $\mathcal{M} = \mathbb{R}^d$ equipped with the standard Euclidean 2-norm, and if the map s is linear, McCann’s polar factorization theorem reduces to polar decomposition of matrices (see Brenier [1991]), namely:

$$s(\mathbf{x}) = \mathbf{S}\mathbf{x} = \mathbf{T}\mathbf{U}\mathbf{x} \quad (12)$$

where $\mathbf{x} \in \mathbb{R}^d$, $\mathbf{S} \in \mathbb{R}^{d \times d}$ is invertible, $\mathbf{T} = (\mathbf{S}\mathbf{S}^T)^{\frac{1}{2}} > 0$, and $\mathbf{U} = \mathbf{T}^{-1}\mathbf{S}$ is unitary. Theorem 1 in Courty et al. [2017] states that the map $t(\mathbf{x}) = \mathbf{T}\mathbf{x} + \mathbf{b}$ with any $\mathbf{b} \in \mathbb{R}^d$ is the solution to an OT problem between an (atomic) measure μ_1 and $\mu_2 = \mu_1 \circ t^{-1}$. Using the polar factorization theorem in the Euclidean case described above, we can provide a new alternative proof to Theorem 1 for the continuous case. Let $\mathbf{T} > 0$ and consider the function $\psi(\mathbf{x}) = \frac{1}{2}\mathbf{x}^T\mathbf{T}\mathbf{x} + \mathbf{b}^T\mathbf{x}$. Since $\mathbf{T} > 0$, ψ is c -convex with respect to the cost $c(\mathbf{x}, \mathbf{z}) = \|\mathbf{x} - \mathbf{z}\|_2^2$. In addition, $\nabla\psi = t$, and therefore, by the polar factorization theorem, the map $t(\mathbf{x}) = \mathbf{T}\mathbf{x} + \mathbf{b}$ is the solution to the OT problem.

In this work we focus on the cone manifold of SPD matrices \mathcal{P}_d . Consider the following general linear map on \mathcal{P}_d , with a fixed, real-valued, invertible matrix \mathbf{S} :

$$s(\mathbf{P}) = \mathbf{S}\mathbf{P}\mathbf{S}^T. \quad (13)$$

Using the polar decomposition $\mathbf{S} = \mathbf{T}\mathbf{U}$ we can write $s(\mathbf{P}) = \mathbf{T}\mathbf{U}\mathbf{P}\mathbf{U}^T\mathbf{T}$. We now show that in analogy to the Euclidean case, the map $\mathbf{Q} = t(\mathbf{P}) = \mathbf{T}\mathbf{P}\mathbf{T}$ is the solution to an OT problem between a measure μ_1 and $\mu_2 = \mu_1 \circ t^{-1}$ on \mathcal{P}_d with $c(\mathbf{P}, \mathbf{Q}) = \|\mathbf{P} - \mathbf{Q}\|_F^2$ where $\mathbf{P}, \mathbf{Q} \in \mathcal{P}_d$.

Using the $\text{vec}(\cdot)$ operator we can write $\mathbf{q} = (\mathbf{T} \otimes \mathbf{T})\mathbf{p}$, where $\mathbf{q} = \text{vec}(\mathbf{Q})$, $\mathbf{p} = \text{vec}(\mathbf{P})$, and \otimes is the Kronecker product. Since $\mathbf{T} > 0$, then $(\mathbf{T} \otimes \mathbf{T}) > 0$ as well. Therefore $t(\mathbf{p}) = (\mathbf{T} \otimes \mathbf{T})\mathbf{p}$ is the solution to the OT problem between μ_1 and $\mu_2 = \mu_1 \circ t^{-1}$ with the given cost function.

We conjecture that in this linear case the map t is the solution to the OT problem on \mathcal{P}_d with $c(\mathbf{P}, \mathbf{Q}) = d_R^2(\mathbf{P}, \mathbf{Q})$ as well. We leave the proof for future work, yet, in the following, we present empirical evidence supporting this conjecture. More importantly, in the general case, the OT plan obtained using the Euclidean distance could be substantially different from the OT plan obtained using the Riemannian distance d_R as demonstrated in Section 4.

3.3 Domain adaptation on the cone manifold of SPD matrices

Consider two sets of SPD matrices in \mathcal{P}_d , source $\{\mathbf{P}_i\}_{i=1}^{N_1}$ and target $\{\mathbf{Q}_i\}_{i=1}^{N_2}$, residing in two different domains. Our goal is to find a map from the source domain to the target domain, such that after applying the mapping to the source set, the two sets live in the same domain, while preserving important and relevant information.

Following Courty et al. [2017], we propose to find such a map using OT. With the above preparation, we start by showing an equivalence in the linear case between applying OT to data in a Euclidean space, which is the common practice, and applying OT to their covariance matrices. Consider a set of matrices $\{\mathbf{X}_i\}_{i=1}^N$ in $\mathbb{R}^{d \times M}$, and denote the empirical covariance matrix of \mathbf{X}_i by \mathbf{P}_i . Consider the linear map $\mathbf{Z}_i = \mathbf{S}\mathbf{X}_i = \mathbf{T}\mathbf{U}\mathbf{X}_i$ using the polar decomposition as in (12). Consequently, the covariance of \mathbf{Z}_i is given by $\mathbf{Q}_i = \mathbf{S}\mathbf{P}_i\mathbf{S}^T = \mathbf{T}\mathbf{U}\mathbf{P}_i\mathbf{U}^T\mathbf{T}$ as in (13). By Section 3.2, if $\mathbf{S} > 0$, namely \mathbf{U} is the identity matrix and $\mathbf{S} = \mathbf{T}$, then, by applying OT to $\{\mathbf{P}_i\}_{i=1}^N$ and $\{\mathbf{Q}_i\}_{i=1}^N$, the obtained mapping t satisfies $t(\mathbf{P}_i) = \mathbf{Q}_i$. Similarly, applying OT to $\{\mathbf{X}_i\}_{i=1}^N$ and $\{\mathbf{Z}_i\}_{i=1}^N$ yields the equivalent map \tilde{t} , such that $\tilde{t}(\mathbf{X}_i) = \mathbf{Z}_i$.

The above discussion highlights two shortcomings of typical OT schemes applied directly to data in a Euclidean space for the purpose of domain adaptation. First, if $M \gg d$, then the pairwise distances are computed in a high-dimensional space, whereas, by exploiting the symmetry of the covariance, the dimension of the matrix is $d(d+1)/2$. Second, and more importantly, with the Euclidean distance, we completely ignore the covariance geometry leading to subpar performance. By considering OT with the Riemannian distance d_R on \mathcal{P}_d , we incorporate the geometric structure, which facilitates meaningful comparisons and enables us to achieve state of the art performance in applications, as we demonstrate in Section 4.2 and Section 4.3.

3.4 Proposed method

The proposed approach for domain adaptation on \mathcal{P}_d is given in Algorithm 1. The algorithm maps a source set $\{\mathbf{P}_i\}_{i=1}^{N_1}$ to the domain of a target set $\{\mathbf{Q}_i\}_{i=1}^{N_2}$ and is comprised of three main steps: (i) setting the histograms, (ii) solving OT, and (iii) applying the transport plan.

In the remainder of this section, we outline several implementation remarks. First, setting the histograms uniformly, namely, $p[i] = 1/N_1$, and $q[j] = 1/N_2$ for $i \in \{1, 2, \dots, N_1\}$ and $j \in \{1, 2, \dots, N_2\}$, is common practice. Yet, our numerical experiments consistently showed that Algorithm 1 is more stable and robust when setting the histograms using Kernel Density Estimation (KDE). Concretely, Step 1 is replaced by $p[i] = \frac{1}{Z} \sum_{j=1}^{N_1} \exp\left(\frac{d_R^2(\mathbf{P}_i, \mathbf{P}_j)}{2\sigma^2}\right)$, where $Z \in \mathbb{R}$ is set such that $\sum_{i=1}^{N_1} p[i] = 1$ and σ^2 is usually set around the median of $\{d_R^2(\mathbf{P}_i, \mathbf{P}_j)\}_{i,j}$. Step 2 for the histogram q is modified in an analogous fashion. Second, we propose to obtain the transport plan Γ in an unsupervised setting, by using the Sinkhorn OT algorithm presented by Cuturi [2013]. In a supervised setting, when the labels of the source set are known, Step 4 can be replaced with the regularized version of the optional transport proposed by Courty et al. [2014]. We refer the readers to the Supplementary Material (SM) for brief descriptions of the algorithms.

The final remark concerns the implementation of Step 5. Step 4 results in the transport plan matrix $\Gamma \in \mathbb{R}^{N_1 \times N_2}$. Courty et al. [2017] proposed to apply domain adaptation in the Euclidean space using the mapping defined by the weighted mean $\hat{x}_i = t(\mathbf{x}_i) = \arg \min_{\mathbf{x} \in \mathbb{R}^n} \sum_j \Gamma[i, j] \|\mathbf{x} - \mathbf{z}_i\|_2^2$. However, when considering a general Riemannian manifold, this quantity might not be well-defined, since the Riemannian mean is not necessarily unique. Fortunately, in \mathcal{P}_d , the Riemannian weighted mean is unique and the optimization problem is strictly convex, see Bhatia [2009]. Therefore, Step 5 consists of a well-defined map:

$$\hat{\mathbf{P}}_i = t(\mathbf{P}_i) = \arg \min_{\mathbf{P} \in \mathcal{P}_d} \sum_{j=1}^{N_2} \Gamma[i, j] d_R^2(\mathbf{P}, \mathbf{Q}_j). \quad (14)$$

Fletcher and Joshi [2004] presented a gradient descent based algorithm for computing the Riemannian mean in \mathcal{P}_d . Here, we extend their algorithm to support the computation of a weighted Riemannian mean, which allows us to implement the map in (14). The new algorithm is given in Algorithm 2. In practice, since Γ tends to be sparse, in order to reduce the computational load in Step 5 of Algorithm 1, one can use only the highest values in the i th row of Γ .

Algorithm 1 Domain adaptation using optimal transport on the manifold of SPD matrices

Input: source set $\{\mathbf{P}_i\}_{i=1}^{N_1}$ and target set $\{\mathbf{Q}_j\}_{j=1}^{N_2}$ of SPD matrices.

Output: the adapted source set to the target domain $\{\tilde{\mathbf{P}}_i\}_{i=1}^{N_1}$.

- 1: **for all** i **do:** $p[i] \leftarrow 1/N_1$. ▷ $i \in \{1, \dots, N_1\}$
- 2: **for all** j **do:** $q[j] \leftarrow 1/N_2$. ▷ $j \in \{1, \dots, N_2\}$
- 3: **for all** i and j **do:** $C[i, j] \leftarrow d_R^2(\mathbf{P}_i, \mathbf{Q}_j)$. ▷ see Eq. (3)
- 4: **set:** $\Gamma \leftarrow \text{SinkhornOptimalTransport}(\mathbf{p}, \mathbf{q}, \mathbf{C})$. ▷ see Section 3.4
- 5: **for all** i **do:** ▷ see Section 3.4

$$\tilde{\mathbf{P}}_i \leftarrow t(\mathbf{P}_i) = \arg \min_{\mathbf{P} \in \mathcal{P}_d} \sum_{j=1}^{N_2} \Gamma[i, j] d_R^2(\mathbf{P}, \mathbf{Q}_j)$$

Algorithm 2 Weighted Riemannian mean

Input: a set of SPD matrices $\{\mathbf{P}_i\}_{i=1}^N$ and non-negative weights $\{w_i\}_{i=1}^N$ such that $\sum_i w_i = 1$.

Output: the weighted Riemannian mean $\bar{\mathbf{P}}$ satisfying $\bar{\mathbf{P}} = \arg \min_{\mathbf{P} \in \mathcal{P}_d} \sum_i w_i d_R^2(\mathbf{P}, \mathbf{P}_i)$.

- 1: **set:** $\bar{\mathbf{P}} \leftarrow \frac{1}{N} \sum_{i=1}^N w_i \mathbf{P}_i$. ▷ starting point
- 2: **do:**
- 3: **update:** $\bar{\mathbf{S}} \leftarrow \frac{1}{N} \sum_{i=1}^N w_i \text{Log}_{\bar{\mathbf{P}}}(\mathbf{P}_i)$. ▷ weighted Euclidean mean in $\mathcal{T}_{\bar{\mathbf{P}}}\mathcal{P}_d$, see (4)
- 4: **update:** $\bar{\mathbf{P}} \leftarrow \text{Exp}_{\bar{\mathbf{P}}}(\bar{\mathbf{S}})$. ▷ see (5)
- 5: **while** $\|\bar{\mathbf{S}}\|_F > \epsilon$ ▷ $\|\cdot\|_F$ is the Frobenius norm

4 Experimental results

In this section we first present a toy example, illustrating the matrix polar decomposition and the subsequent conjecture described in Section 3.2. Then, we present results on two BCI data sets, where our method achieves state of the art classification performance. Our source code is available in the SM and will be publicly available on github upon acceptance. Additional implementation details are given in the SM.

4.1 Toy problem

Any symmetric 2×2 matrix $\mathbf{A} = \begin{bmatrix} x & y \\ y & z \end{bmatrix}$ can be visualized in \mathbb{R}^3 by plotting the elements (x, y, z) . In addition, \mathbf{A} is positive-definite if and only if $x, z > 0$ and $y^2 < xz$. These conditions imply that the 2×2 SPD matrices reside within a cone embedded in \mathbb{R}^3 . Consider a 2×2 SPD matrix \mathbf{P} and a parametric map s_θ given by $s_\theta(\mathbf{P}) = \mathbf{S}_\theta \mathbf{P} \mathbf{S}_\theta^T$, where $\mathbf{S} = \mathbf{T} \mathbf{U}_\theta$, $\mathbf{T} = \begin{bmatrix} 0.5 & -1/4 \\ -1/4 & 1 \end{bmatrix} > 0$ and $\mathbf{U}_\theta = \begin{bmatrix} \cos(\theta) & \sin(\theta) \\ -\sin(\theta) & \cos(\theta) \end{bmatrix}$ is unitary.

First, we generate a set of 5 SPD matrices $\{\mathbf{P}_i\}_{i=1}^5$ and apply s_0 and $s_{\pi/2}$ to this set. The pairs $(\mathbf{P}_i, s_\theta(\mathbf{P}_i))$ embedded in \mathbb{R}^3 are depicted in Figure 1(a and b). In the left plots, the pairs are connected by the geodesic curves. In the right plots, the curves represent the matching obtained by t_θ computed using Algorithm 1. In Figure 1(a), where $\mathbf{S}_0 = \mathbf{T} > 0$ and does not contain a unitary component, we observe that the obtained OT recovers the map s_0 . Conversely, in Figure 1(b), where $\mathbf{S}_{\pi/2}$ has a non-trivial unitary component, we observe that the OT *does not recover* the true matching.

To further quantify this observation, we generate a set of $N = 50$ SPD matrices $\{\mathbf{P}_i\}_{i=1}^N$ and consider the map s_θ , where $\theta \in [0, \pi]$. For each value of θ , we compute t_θ using Algorithm 1. Figure 1(c) displays the error between $s_\theta(\mathbf{P}_i)$ and the corresponding $t_\theta(\mathbf{P}_i)$ defined by $\sqrt{\frac{1}{N} \sum_{i=1}^N d_R^2(t_\theta(\mathbf{P}_i), s_\theta(\mathbf{P}_i))}$. In addition, Figure 1(d) presents the transport plans Γ obtained for 4 values of θ . Indeed, we observe that the ability of OT to recover s_θ depends on θ ; as the unitary component of s_θ is ‘less prominent’ (θ is closer to 0), the recovery becomes more accurate.

4.2 Motor imagery task

We use data from the BCI competition IV, see Naeem et al. [2006], which have been previously addressed using the Riemannian geometry of SPD matrices by Barachant et al. [2012], Zanini et al. [2018], and Yair et al. [2019]. The dataset contains EEG recordings from 22 electrodes from 9 subjects, where each subject was recorded in 2 different days (sessions). In repeated trials, the subjects were asked to imagine performing one out of four possible movements: (i) right

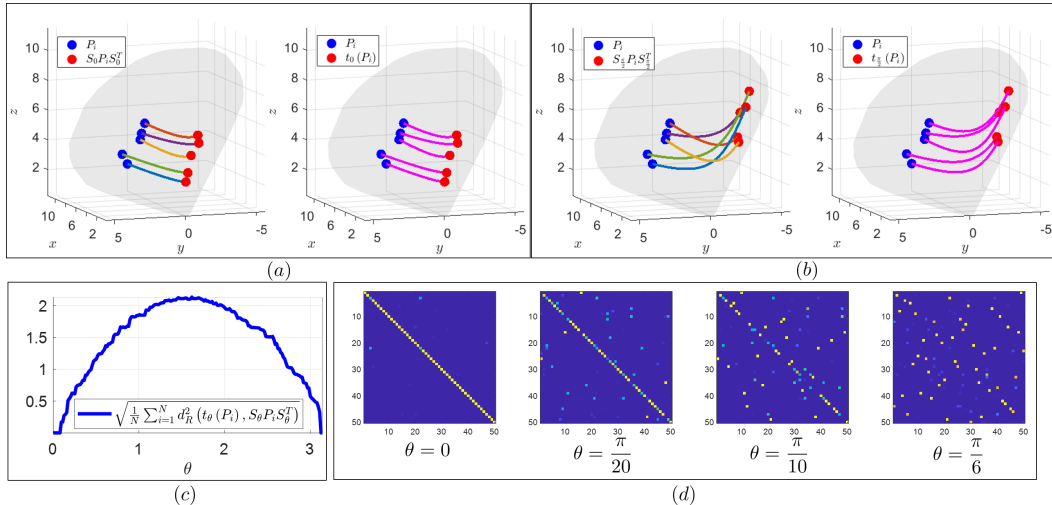


Figure 1: Results on the toy problem, please see Section 4.1 for details.

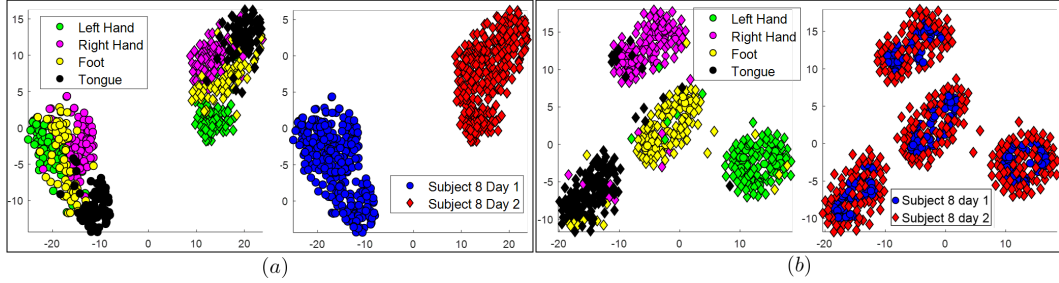


Figure 2: Cross-session adaptation in the motor imagery task. The t-SNE representation of all the SPD matrices of Subject 8: (a) before Algorithm 1 and (b) after. Please see Section 4.2 for details.

Table 1: Classification accuracy in the motor imagery task

(a) Cross-session accuracy

Sub.	Alg. 1	PT	AT	Ang at el.
1	82.29	81.25	79.6	67.6
3	88.19	88.19	81.5	74.5
7	78.47	76.39	75.2	77.3
8	85.07	82.99	82.1	75.5
9	85.42	77.78	81.8	60.6
Mean	83.89	81.32	80	71.1

(b) Cross-subject accuracy

Sub.	Alg. 1	Euclid	PT	AT
1	67.88	61.98	60.31	60.4
3	75.52	70.40	65.02	69.4
7	64.76	60.85	57.03	57.0
8	68.92	65.97	59.81	63.2
9	66.75	56.43	63.63	68.8
Mean	68.92	63.13	61.16	63.76

hand, (ii) left hand, (iii) both feet, and (iv) tongue. Overall, in a single day, each movement was repeated 72 times by each subject. The sampling rate is 250Hz and each trial is 3 second long. Let $\mathbf{X}_i^{(k,s)} \in \mathbb{R}^{22 \times 750}$ denote the data from the i th trial of the k th subject at the s th session, and let $y_i^{(k,s)} \in \{\text{right hand, left hand, both feet, tongue}\}$ be the associated label. For each trial we compute the empirical covariance matrix $\mathbf{P}_i^{(k,s)} \in \mathbb{R}^{22 \times 22}$. To illustrate the need for domain adaptation, Figure 2(a) displays the 2-D t-SNE representation (presented by Maaten and Hinton [2008]) of all the SPD matrices of Subject 8, namely $\{\mathbf{P}_i^{(8,s)}\}, i = 1, \dots, 288, s = 1, 2$, computed based on the pairwise distances d_R . We observe that the data is primarily clustered by the session, whereas the clustering by the imagined movement is only secondary. This poses a challenge for classifiers trained on one session and applied to the other. We adapt the SPD matrices of the first session by Algorithm 1; let $\{\tilde{\mathbf{P}}_i^{(8,1)}\}$ denote the output of the algorithm. Figure 2(b) depicts the 2-D t-SNE representation of $\{\tilde{\mathbf{P}}_i^{(8,1)}\}$. Now we observe that the data is primarily clustered by the imagined movement, whereas as the session has only a mild effect. See the SM for more results including a completely unsupervised adaptation as well as multiple cross-subject adaptation.

To quantify the adaptation, we present the classification accuracy for cross-session and cross-subject classification. We compare the performance to three methods: (i) the method by Ang et al. [2012] which achieved the 1st place in the original competition, (ii) the Affine Transform (AT) proposed by Zanini et al. [2018], and (iii) the Parallel Transport (PT) proposed by Yair et al. [2019]. For evaluation, we use a linear SVM classifier equipped with the Euclidean approximation (7). Table 1(a) depicts the cross-session performance and Table 1(b) depicts the cross-subject performance. Note that the results by Ang et al. [2012] are available only for the cross-session case. In addition, in the cross-subject case, we added a variant of Algorithm 1, which relies on the Euclidean distance instead of the Riemannian distance (labeled ‘‘Euclid’’). We observe that overall Algorithm 1 provides the best results. See the SM for the complete Table 1(b). We consider only 5 subjects out of the available 9 as in Zanini et al. [2018] and Yair et al. [2019]. This is because the single-session single-subject classification results on data from each of the remaining 4 subjects were poor, see Ang et al. [2012], Barachant et al. [2012], Zanini et al. [2018]. Thus, domain adaption is not relevant.

Table 2: Classification precision in the ERP P300 task

Train sub.	1	2	3	4	5	6	Alg. 1	PT	AT
Test sub.	1	2	3	4	5	6	Alg. 1	PT	AT
1	93.94	93.94	90.91	92.68	86.36	91.57	93.31	86.3	
2	96.77		90.91	91.43	93.94	75.51	89.71	89.55	85.8
3	97.73	97.87		95.56	95.56	95.35	96.05	91.44	N/A
4	97.06	100	100		95.83	97.44	98.07	91.45	N/A
5	98.21	96.49	93.94	98.36		93.33	96.07	90.35	86.7
6	88.37	85.71	76.60	84.00	92.50		85.44	69.17	89.6
Mean							92.82	87.55	87.1

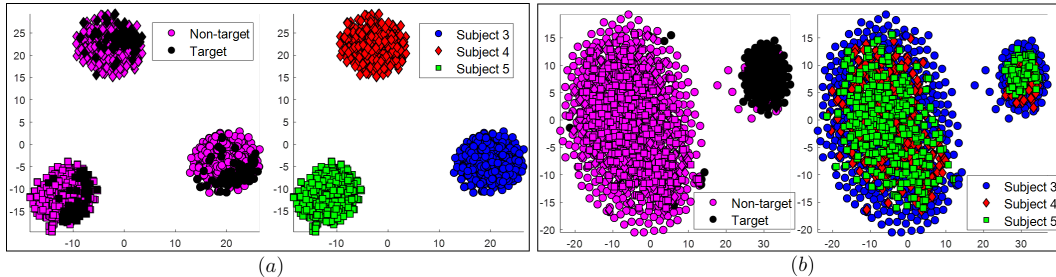


Figure 3: Cross-subject adaptation in the ERP P300 task. The t-SNE representation of the SPD matrices of three subjects: (a) before Algorithm 1 and (b) after. Please see Section 4.3 for details.

4.3 Event related potential P300 task

We use data from the Brain Invaders experiment from GIPSA-lab. Here we only include a brief description; for more details see Congedo et al. [2011]. In this experiment, subjects watched a screen with 36 objects flashing alternatively. Their task was to mentally count the number of flashes of the specific (a-priori known) target objects. Spotting a target generates a *P300* wave, which is an Event Related Potential (ERP). Each subject watched 480 trials, of which 80 contained the target and the remaining 400 did not. The data consist of EEG recordings from 16 electrodes sampled at 512Hz. The duration of each trial is one second. Note that the empirical covariance matrix is invariant to the temporal order of the samples, yet the ERP is a short local wave. Consequently, the covariance matrix does not capture sufficient information on the ERP in a given trial. Thus, instead of the standard covariance matrix, we use an augmented covariance matrix as proposed by Barachant and Congedo [2014] based on concatenating artificial channels to the data. While Zanini et al. [2018] used the true hidden labels for that purpose, we apply a more practical approach which does not require access to the hidden labels. See the SM for details.

To illustrate the existing batch effect in the data, and subsequently, the need for domain adaptation, Figure 3(a) displays the 2-D t-SNE representation of data from three subjects (3, 4 and 5). As in the previous application, we observe that the SPD matrices are primarily clustered by the subject. Figure 3(b) displays the data from the same three subjects after applying Algorithm 1 to adapt the SPD matrices of Subject 4 and Subject 5 to the domain of the SPD matrices of Subject 3. We now observe that the SPD matrices are clustered by the label of the trial and not by the subjects. See the SM for additional results.

To quantify the adaptation, we present the cross-subject classification precision, defined by $\text{pr} = \frac{\text{TP}}{\text{TP} + \text{FP}}$, where TP is the number of trials with target objects correctly classified and FP is the number of trials without a target wrongly classified as with a target. We compare Algorithm 1 to the algorithms presented by Zanini et al. [2018] and by Yair et al. [2019]. For the comparison, we use the same Minimum Distance to Mean (MDM) classifier as in Zanini et al. [2018], which was proposed by Barachant et al. [2012]. Table 2 contains the classification precision obtained by Algorithm 1 and the summary of the mean performance of the algorithms. The N/A results were not reported by Zanini et al. [2018], since these subjects were classified as “bad” subjects. We observe that Algorithm 1 provides the best results overall.

5 Conclusion

In this paper we presented an approach (and the resulting algorithm) for domain adaptation on the cone manifold of SPD matrices using OT. Based on the polar factorization theorem, we stated the conditions for successful mapping and the limitations of this mapping when the conditions are not met. The mapping we derived is well-defined, and we presented an algorithm for its simple implementation. Our method achieves state of the art performance in BCI tasks.

Supplementary material

A Source code

Our source code will be publicly available on github upon acceptance. Please notice that in order to apply the code to the data sets, they need to be downloaded first from the following links.

A.1 Motor imagery task

- The data is available [here](#) (data set 2a) and described [here](#).
- We read the data files using [BioSig](#).

A.2 Event related potential P300 task

- The data is available [here](#) and described [here](#).
- We used the [py.BI.EEG.2012-GIPSA](#) repository to read the data files and to save them in ‘.mat’ format.
- For computing the appended covariance features, we used this [this](#) P300 detector.

B Regularized optimal transport algorithms

In Algorithm 1 in the paper, Step 4 solves the OT problem. In this section, we document two possible fast implementations of a regularized version of the classical OT. The first implementation is completely unsupervised, whereas, the second implementation supports a supervised configuration, where the labels of the source set are known.

B.1 Classical optimal transport

Given two discrete density vectors, source $\mathbf{c} \in \mathbb{R}^{N_1}$ and target $\mathbf{r} \in \mathbb{R}^{N_2}$, as well as the cost matrix $\mathbf{C} \in \mathbb{R}^{N_1 \times N_2}$, the discrete version of optimal transport is the following optimization problem:

$$\arg \min_{\Gamma} \langle \Gamma, \mathbf{C} \rangle \quad (15)$$

such that $\Gamma \mathbf{1} = \mathbf{c}$ and $\Gamma^T \mathbf{1} = \mathbf{r}$, where $\mathbf{1}$ is a vector of all ones with a suitable dimension.

B.2 Sinkhorn optimal transport

Often, the computation cost of (15) becomes extremely high when the dimensions N_1 and N_2 exceed several hundreds. Cuturi [2013] proposed to solve the optimal transport problem with a regularization term based on entropy, which can be computed with the Sinkhorn's matrix scaling algorithm at a speed that is several orders of magnitude faster than that of classical optimal transport solvers. The proposed regularized problem is:

$$\arg \min_{\Gamma} \langle \Gamma, \mathbf{C} \rangle - \frac{1}{\lambda} h(\Gamma) \quad (16)$$

where $h(\Gamma) = - \sum_{i=1}^{N_1} \sum_{j=1}^{N_2} \Gamma[i, j] \log(\Gamma[i, j])$ is the entropy of Γ . We note that in the toy problem in Section 4.1 we assign large values to λ , so that the regularized problem (16) is similar to the classical problem (15). For the real data sets in Section 4.2 and Section 4.3, we set λ adaptively by

$$\lambda = \frac{1}{2m^2}$$

where $m = 0.05 \cdot \text{median}\{\mathbf{C}[i, j]\}_{i,j}$. We implemented Algorithm 3, which was proposed by Cuturi [2013] and solves (16), as outlined below.

Algorithm 3 Sinkhorn optimal transport proposed by Cuturi [2013]

Input: $\mathbf{C} \in \mathbb{R}^{N_1 \times N_2}$, $\lambda \in \mathbb{R}$, $\mathbf{c} \in \mathbb{R}^{N_1}$, and $\mathbf{r} \in \mathbb{R}^{N_2}$.

Output: the transport plan $\Gamma \in \mathbb{R}^{N_1 \times N_2}$ (solution of (16)).

```

1: set:  $\mathbf{K}[i, j] \leftarrow \exp(-\lambda \mathbf{C}[i, j])$   $\triangleright \forall i \in \{1, \dots, N_1\}$  and  $\forall j \in \{1, \dots, N_2\}$ 
2: set:  $\mathbf{u}[i] \leftarrow \frac{1}{N_1}$   $\triangleright \forall i \in \{1, \dots, N_1\}$ 
3: set:  $\tilde{\mathbf{K}}[i, j] \leftarrow \frac{\mathbf{K}[i, j]}{\mathbf{c}[i]}$   $\triangleright \forall i \in \{1, \dots, N_1\}$  and  $\forall j \in \{1, \dots, N_2\}$ 
4: while  $\mathbf{u}$  changes do
5:    $\mathbf{z}[j] \leftarrow \frac{\mathbf{r}[j]}{(\mathbf{K}^T \mathbf{u})[j]}$   $\triangleright \forall j \in \{1, \dots, N_2\}$ 
6:   update:  $\mathbf{u}[i] = \frac{1}{(\tilde{\mathbf{K}} \mathbf{z})[i]}$   $\triangleright \forall i \in \{1, \dots, N_1\}$ 
7: end while
8: set:  $\mathbf{v}[j] \leftarrow \frac{\mathbf{r}[j]}{(\mathbf{K}^T \mathbf{u})[j]}$   $\triangleright \forall j \in \{1, \dots, N_2\}$ 
9: set:  $\Gamma \leftarrow \text{diag}(\mathbf{u}) \mathbf{K} \text{diag}(\mathbf{v})$ 

```

B.3 Sinkhorn optimal transport with labels

Consider now a supervised setting consisting of two sets of SPD matrices in \mathcal{P}_d . The source set $\{\mathbf{P}_i, y_i\}_{i=1}^{N_1}$ is given with labels $y_i \in \mathcal{Y}$, where \mathcal{Y} is the set of all possible labels, and the target set $\{\mathbf{Q}_i\}_{i=1}^{N_2}$ is unlabeled (i.e., the labels are unknown). We set $\mathbf{C}_0[i, j] = d_R^2(\mathbf{P}_i, \mathbf{Q}_j)$. Courty et al. [2014] presented a modification of the Sinkhorn optimal transport problem with an additional label regularization term and derived a new efficient algorithm to solve the following problem:

$$\arg \min_{\Gamma} \langle \Gamma, \mathbf{C}_0 \rangle - \frac{1}{\lambda} h(\Gamma) + \eta \sum_{j=1}^{N_2} \sum_{y=1}^{|\mathcal{Y}|} \|\Gamma(\mathcal{I}_y, j)\|_q^p \quad (17)$$

where \mathcal{I}_y is a set containing the indices of the source points associated with the label $y \in \mathcal{Y}$, $\Gamma(\mathcal{I}_y, j)$ is a vector consisting of entries from the j th column of Γ associated with the label y (i.e., from rows \mathcal{I}_y) and $\|\cdot\|_q^p$ is the ℓ_q norm to the power of p . See Courty et al. [2014] for more details. We implemented Algorithm 4, which was proposed by Courty et al. [2014] and solves (17), as outlined below.

Algorithm 4 Sinkhorn optimal transport with labels proposed by Courty et al. [2014]

Input: $C_0 \in \mathbb{R}^{N_1 \times N_2}$, $\lambda \in \mathbb{R}$, $c \in \mathbb{R}^{N_1}$, $r \in \mathbb{R}^{N_2}$, and the source labels $\{y_i\}_{i=1}^{N_1}$.

Output: the transport plan Γ (solution of (17)).

1: **initialize:** $G \leftarrow \mathbf{0}$ $\triangleright G \in \mathbb{R}^{N_1 \times N_2}$
 2: **do**
 3: **update** $C \leftarrow C_0 + G$
 4: **update** $\Gamma \leftarrow \text{SinkhornOptimalTransport}(C, \lambda, c, r)$ \triangleright Algorithm 3
 5: **update** G according to $\triangleright \forall y$ and $\forall j$

$$G(\mathcal{I}_y, j) \leftarrow p \cdot (\|\Gamma(\mathcal{I}_y, j)\| + \epsilon)^{p-1}$$

 6: **while** Γ changes

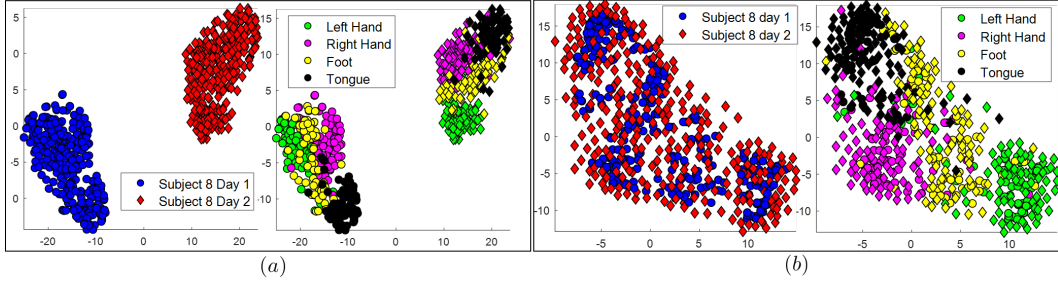


Figure 4: Unsupervised single subject domain adaptation of the data from the BCI motor imagery task. (a) 2-dimensional t-SNE representation of all the SPD matrices of Subject 8. (b) 2-dimensional t-SNE representation of all the SPD matrices of Subject 8 after applying Algorithm 1 without labels.

C Additional comments and results

C.1 Toy problem

For the toy problem in Section 4.1, we used Algorithm 1 in the paper, where Step 4 was implemented with Algorithm 3. High value was assigned to the hyperparameter λ ($\lambda \approx 50$), so that the regularized problem (16) is similar to the classical problem (15). This similarity was desirable since the main purpose of the toy problem is to support the theoretical claims, which relate to the classical problem. Note that when running the toy example code, increasing λ too much might cause numerical issues.

We note that the tested SPD matrices were generated by randomly generating a 2×2 matrix \mathbf{M} , where each entry is normally distributed, and then, we computed $\mathbf{P} = \mathbf{M}\mathbf{M}^T + 0.1\mathbf{I}_{2 \times 2} > 0$.

C.2 Motor imagery task

Prior to computing the covariance matrices, we applied a band pass filter with cutoff frequencies 8Hz and 30Hz (see the ‘GetEvents.m’ script for the implementation). This preprocessing was performed in the previous works by Barachant et al. [2012], Zanini et al. [2018], Yair et al. [2019], where this data set was used.

In the paper, we provide an illustrative result to the cross-session task using the algorithm with labels, namely, we apply Algorithm 1 where Step 4 is implemented using Algorithm 4. For completeness, we now present additional results for multiple subjects obtained both by using Algorithm 4 and by Algorithm 3.

We start by repeating the single subject example reported in Section 4.2 Figure 2 using Algorithm 3 instead of Algorithm 4. Figure 4(a) displays the 2-dimensional t-SNE representation of all the SPD matrices of subject 8, namely $\{\mathbf{P}_i^{(8,s)}\}_{i,s}$, $i = 1, \dots, 288$, $s = 1, 2$. We observe that the data is primarily clustered by the session, whereas the clustering by the imagined movement is only secondary. We adapt the representation of the data from the first session by Algorithm 1 (without labels); let $\{\tilde{\mathbf{P}}_i^{(8,1)}\}_i$ denote the output of the algorithm. Figure 4(b) depicts the 2-dimensional t-SNE representation of $\{\tilde{\mathbf{P}}_i^{(8,1)}\}_i$. Similarly to the result from the paper, we observe that the data is primarily clustered by the imagined movement, whereas as the session is only mildly noticeable. In contrast to the result reported in the paper, this result was obtained in a completely unsupervised manner.

Next, we test the adaptation of five sets corresponding to all subjects¹. One set corresponding to Subject 1 was set as the reference set. Then, we applied Algorithm 1 to the remaining sets of the 4 subjects, mapping them one by one to the reference set. Figure 5(a) displays the 2-dimensional t-SNE representation to the SPD matrices of all five subjects (in session 1). Figure 5(b) displays the 2-dimensional t-SNE representation of the SPD matrices after applying Algorithm 1, where Step 4 was implemented using Algorithm 4. In addition, Figure 6 is similar to Figure 5, where the difference is that Algorithm 3 was applied in Step 4 instead. Namely, this result is obtained in an unsupervised manner.

Finally, Table 3 provides the cross-subject classification accuracy, extending Table 1(b), which appears in Section 4.2.

¹As reported in the paper, we consider only 5 subject out of the available 9. See the explanation in Section 4.2 for details.

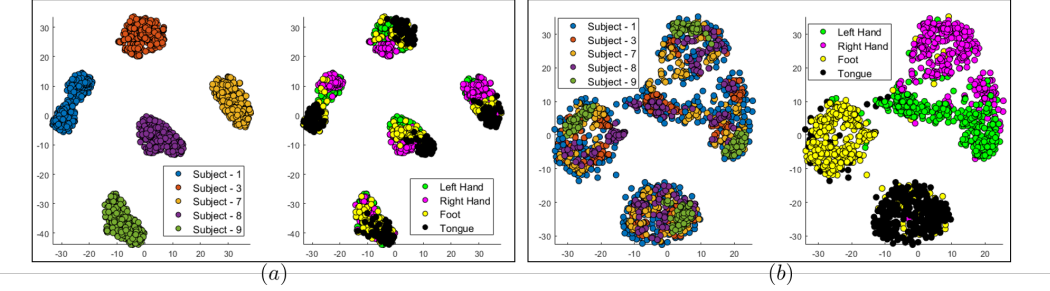


Figure 5: Supervised multi-subject domain adaptation of the data from the BCI motor imagery task. (a) 2-dimensional t-SNE representation of all the SPD matrices of all five subjects (in Session 1). (b) 2-dimensional t-SNE representation of all the SPD matrices of the five subjects after applying Algorithm 1 with labels.

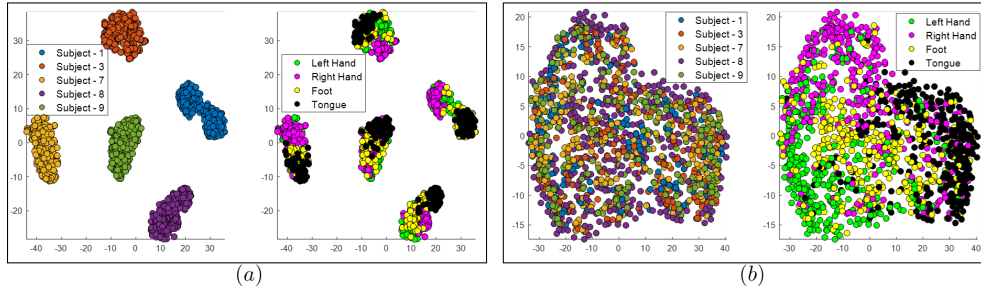


Figure 6: Unsupervised multi-subject domain adaptation of the data from the BCI motor imagery task. (a) 2-dimensional t-SNE representation of all the SPD matrices of all five subjects (in Session 1). (b) 2-dimensional t-SNE representation of all the SPD matrices of the five subjects after applying Algorithm 1 without labels.

Table 3: Cross-subject classification accuracy in the motor imagery task. The four right-most columns consist of the mean results obtained per subject. Alg. 1 stands for Algorithm 1, Alg. 1 (Euclid) stands for Algorithm 1 when the Euclidean distance is used instead of the Riemannian distance d_R . PT stands for domain adaptation using Parallel Transport by Yair et al. [2019]. AT stands for the domain adaptation using Affine Transform by Zanini et al. [2018].

Test sub.	Train sub.	1	3	7	8	9	Alg. 1	Alg. 1 (Euclid)	PT	AT
1			78.13	67.36	70.14	55.90	67.88	61.98	60.31	60.4
3		78.13		79.17	78.13	66.67	75.52	70.40	65.02	69.4
7		63.54	70.49		62.50	68.40	64.76	60.85	57.03	57.0
8		68.06	72.22	67.01		66.32	68.92	65.97	59.81	63.2
9		52.43	67.36	72.22	75.00		66.75	56.43	63.63	68.8
Mean							68.92	63.13	61.16	63.76

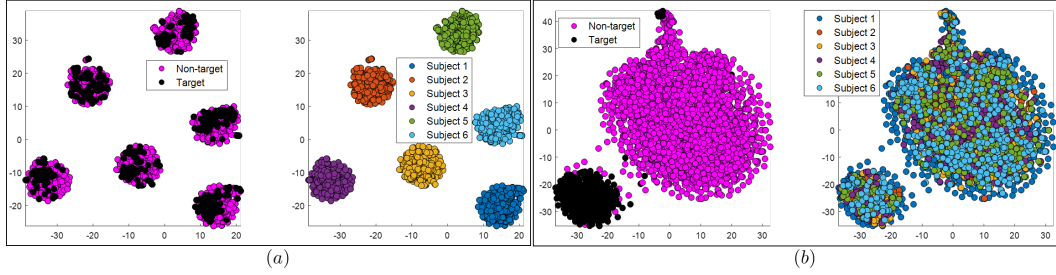


Figure 7: Supervised multi-subject domain adaptation of the data from the ERP P300 task. (a) 2-dimensional t-SNE representation of all the SPD matrices of all six subjects. (b) 2-dimensional t-SNE representation of all the SPD matrices of the six subjects after applying Algorithm 1 with labels.

C.3 Event related potential P300 task

Prior to computing the covariance matrices, we applied a band pass filter with cutoff frequencies 1Hz and 24Hz. This preprocessing is implemented in the py.BI.EEG.2012-GIPSA github code. A similar preprocessing was also applied by Barachant and Congedo [2014].

This data set was previously tested by Barachant and Congedo [2014], where it was realized that the ordinary covariance matrices are insufficient. Instead, it was proposed to use an augmented version of the covariance matrices. In Zanini et al. [2018], the augmented covariance matrices were computed as follows. Let $\mathcal{T}^{(k)}$ be trials of the k th subject containing an ERP response. Given $\mathcal{T}^{(k)}$, the average ERP response can be computed by: $\bar{\mathbf{X}}^{(k)} = \frac{1}{|\mathcal{T}^{(k)}|} \sum_{i \in \mathcal{T}^{(k)}} \mathbf{X}_i^{(k)}$. Next, the average response $\bar{\mathbf{X}}^{(k)}$ is appended to the data of each trial, obtaining:

$$\tilde{\mathbf{X}}_i^{(k)} = \begin{bmatrix} \bar{\mathbf{X}}^{(k)} \\ \mathbf{X}_i^{(k)} \end{bmatrix}$$

. Then, the augmented empirical covariance of $\tilde{\mathbf{X}}_i^{(k)}$, denoted by $\tilde{\mathbf{P}}_i^{(k)}$, is computed.

Since this method requires the knowledge of the true hidden labels (which are subsequently estimated), in the current paper, we use a more practical approach, which does not require the hidden labels. For each subject k , we apply the ERP detector proposed by Hoffmann et al. [2005] to all 480 trials. The overall accuracy of this ERP detector was very low and it cannot be used as a stand-alone method for classification of data from multiple subjects. However, when considering only the 15 trials for each subject k with the highest confidence score as trials with an ERP response, we approximate a subset of $\mathcal{T}^{(k)}$, which in turn, we use to compute the augmented covariance matrices. We remark that on average 12 out of the 15 trials indeed include an ERP response.

It is important to note that the entire data set contains 24 subjects. We test our algorithm on 6 six subjects, and we use the remaining 18 subjects to train the P300 detector. Consequently, the P300 detector and the proposed domain adaptation algorithm do not share the same data.

We now provide additional results in which the domain adaptation is tested on all the six subject simultaneously. As in the motor imagery task, the data from Subject 1 is set as a reference, and the data from remaining five subject are adapted (subject by subject) to the reference set. Figure 7(a) displays the 2-dimensional t-SNE representation of all the SPD matrices of the six subjects. Figure 7(b) depicts the 2-dimensional t-SNE representation of the SPD matrices after applying Algorithm 1 with Algorithm 4 at Step 4. Figure 8 is similar to Figure 7, where the difference is that Algorithm 3 was applied in Step 4 instead. Namely, this result is obtained in an unsupervised manner.

References

- X. Pennec, P. Fillard, and N. Ayache. A riemannian framework for tensor computing. *International Journal of computer vision*, 66(1):41–66, 2006.
- A. Barachant, S. Bonnet, M. Congedo, and C. Jutten. Classification of covariance matrices using a Riemannian-based kernel for bci applications. *Neurocomputing*, 112:172–178, 2013.
- O. Freifeld, S. Hauberg, and M. J Black. Model transport: Towards scalable transfer learning on manifolds. In *Proceedings of the IEEE Conference on Computer Vision and Pattern Recognition*, pages 1378–1385, 2014.

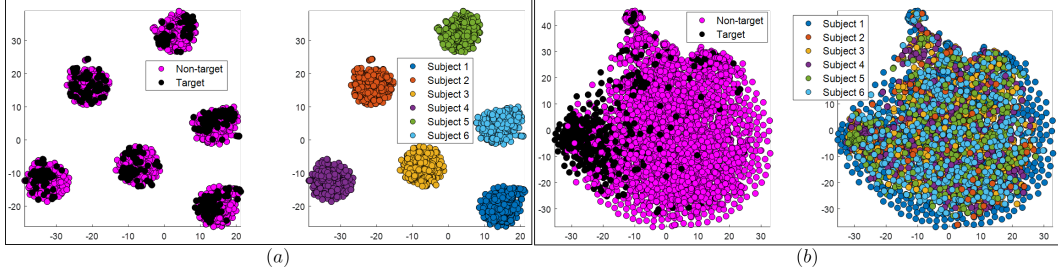


Figure 8: Unsupervised multi-subject domain adaptation of the data from the ERP P300 task. (a) 2-dimensional t-SNE representation of all the SPD matrices of all six subjects. (b) 2-dimensional t-SNE representation of all the SPD matrices of the six subjects after applying Algorithm 1 without labels.

N. Courty, R. Flamary, D. Tuia, and A. Rakotomamonjy. Optimal transport for domain adaptation. *IEEE transactions on pattern analysis and machine intelligence*, 39(9):1853–1865, 2017.

R. Bhatia. *Positive definite matrices*, volume 16. Princeton university press, 2009.

P. T. Fletcher and S. Joshi. Principal geodesic analysis on symmetric spaces: Statistics of diffusion tensors. In *Computer Vision and Mathematical Methods in Medical and Biomedical Image Analysis*, pages 87–98. Springer, 2004.

C. Villani. *Optimal Transport*. Springer Berlin Heidelberg, 2009. doi: 10.1007/978-3-540-71050-9.

A. Fathi and A. Figalli. Optimal transportation on non-compact manifolds. *Israel Journal of Mathematics*, 175(1):1–59, jan 2010. doi: 10.1007/s11856-010-0001-5.

R. McCann. Polar factorization of maps on riemannian manifolds. *Geometric & Functional Analysis GAFA*, 11(3):589–608, 2001.

Y. Brenier. Polar factorization and monotone rearrangement of vector-valued functions. *Communications on Pure and Applied Mathematics*, 44(4):375–417, jun 1991. doi: 10.1002/cpa.3160440402.

K. Modin. Geometry of matrix decompositions seen through optimal transport and information geometry. *Journal of Geometric Mechanics*, 9(3):335–390, jun 2017. doi: 10.3934/jgm.2017014.

M. Cuturi. Sinkhorn distances: Lightspeed computation of optimal transport. In *Advances in neural information processing systems*, pages 2292–2300, 2013.

N. Courty, R. Flamary, and D. Tuia. Domain adaptation with regularized optimal transport. In *Joint European Conference on Machine Learning and Knowledge Discovery in Databases*, pages 274–289. Springer, 2014.

M. Naeem, C. Brunner, R. Leeb, B. Graimann, and G. Pfurtscheller. Separability of four-class motor imagery data using independent components analysis. *Journal of neural engineering*, 3(3):208, 2006.

A. Barachant, S. Bonnet, M. Congedo, and C. Jutten. Multiclass brain–computer interface classification by riemannian geometry. *IEEE Transactions on Biomedical Engineering*, 59(4):920–928, 2012.

P. Zanini, M. Congedo, C. Jutten, S. Said, and Y. Berthoumieu. Transfer learning: a riemannian geometry framework with applications to brain–computer interfaces. *IEEE Transactions on Biomedical Engineering*, 65(5):1107–1116, 2018.

O. Yair, M. Ben-Chen, and R. Talmon. Parallel transport on the cone manifold of spd matrices for domain adaptation. *IEEE Transactions on Signal Processing*, 67(7):1797–1811, 2019.

L. van der Maaten and G. Hinton. Visualizing data using t-sne. *Journal of machine learning research*, 9(Nov):2579–2605, 2008.

K. Ang, Z. Yang Chin, C. Wang, C. Guan, and H. Zhang. Filter bank common spatial pattern algorithm on bci competition iv datasets 2a and 2b. *Frontiers in neuroscience*, 6:39, 2012.

M. Congedo, M. Goyat, N. Tarrin, G. Ionescu, L. Varnet, B. Rivet, R. Phlypo, N. Jrad, M. Acquadro, and C. Jutten. “brain invaders”: a prototype of an open-source p300-based video game working with the openvibe platform. In *5th International Brain-Computer Interface Conference 2011 (BCI 2011)*, pages 280–283, 2011.

A. Barachant and M. Congedo. A plug&play P300 BCI using information geometry. [arXiv preprint arXiv:1409.0107](https://arxiv.org/abs/1409.0107), 2014.

U. Hoffmann, G. Garcia, J. Vesin, K. Diserens, and T. Ebrahimi. A boosting approach to p300 detection with application to brain-computer interfaces. In *Conference Proceedings. 2nd International IEEE EMBS Conference on Neural Engineering, 2005.*, pages 97–100. IEEE, 2005.